Microstructure-induced hotspots in the thermal and elastic responses of granular media

F. Willot, L. Gillibert, and D. Jeulin
MINES ParisTech, Centre de Morphologie Mathématique, Mathématiques et Systèmes, 35, rue Saint Honoré, 77305 Fontainebleau CEDEX, France. Emails: {francois.willot, luc.gillibert, dominique.jeulin}@cmm.ensmp.fr

This work is a combined analytical and numerical study of the extreme values of the thermal and elastic fields occurring in a propellant composite material, a granular medium containing dense self-assembled spheroidal grains embedded in a matrix. First, a 3D microtomography image of a representative sample is segmented using morphological operators. Second, the local temperature and heat flux in the quasi-static thermal response is computed numerically, making use of the segmented microstructure and of experimental values of the heat conductivity in each phase. Such fields are readily derived by means of a Fast Fourier Transform method. Emphasis is put on the maximum values of the local fields: even at low contrast of properties between the grain and the matrix, the heat flux patterns is made of hot-spot zones located in-between grains that are close to each other with preferential directions. Third, the local extrema of the fields are investigated in the context of linear elasticity. Finally, analytical approximations are examined at low and high contrast of properties, on a simple hard-core model of cylinders, which is tantamount to a 2D granular microstructure.

PACS numbers: 46.04.+b, 46.15.-x, 46.65.+g. Keywords: Homogenization; Thermal conductivity; Representative volume element; Hard-core models; Linear elasticity; Random media

I. INTRODUCTION

It is common to study the physical behaviour of composite materials from the point of view of homogenization, to predict the apparent properties from the microstructure and from the local properties. However it may be crucial to study the impact of the microstructure on local extremal properties of the fields, when they can destroy the integrety of the material. This is the case for instance of damage initiation in heterogeneous materials, due to strain or stress concentrations, as studied in a mortar material [7]. In the case of energetic materials like propellants, the role of possible hot spots in the material was studied mainly in the presence of schocks [6]. In other nonlinear contexts, the microstructure is known to induce strong local interactions, such as in visco-plastic polycristals [25, 26] or elastic-plastic hardening in Boolean microstructures [14]. Additionally, the influence of geometrical parameters such as inclusion aspect ratio and mutual distances in simple (periodic) microstructures was studied numerically and experimentally, is especially important in optical properties, where resonances depend on nano-structural details [11].

The temperature and heat flux, or equivalently the electric potential and electric vector field, in the inner region inbetween two closely touching, perfectly conducting spheres was studied by Jeffrey [12]. In its work, Jeffrey expands the potential in terms of multipoles. This approach allowed McPhedran et al. [19–21], using an asymptotic perturbation method, to draw connections with a square array of cylinders. In this respect, earlier works by Keller [17] showed that the effective conductivities of a square lattice of highly-conducting touching spheres is determined by the sigularities in the inner region between spheres. However, the generalization of such results to more general *random* granular media requires numerical computations. In the present paper, we study the initiation in the microstructure of a propellant material of hot spots, by application of a macroscopic thermal gradient or of a macroscopic strain loading. This work combines 3D image segmentation of a large size microtomography obtained on a propellant material, FFT calculation of thermal and elastic fields on the segmented image, image analysis of the fields, and approximate semi-analytical solutions for the fields. Specifically, the article is organized as follow: segmentation techniques are presented in Sec. II, the effective behavior as predicted numerically is discussed in Secs. III and IV, the local fields are investigated in Sec. V, analytical results relevant for the fields maxima at low contrast of properties are given in Sec. VI, and finally the local fields properties at high contrasts are investigated in Secs. VII and VIII.

II. GRANULAR MICROSTRUCTURE AND IMAGE SEGMENTATION

A. Microtomography image

A granular medium known as butalite propellant material is made of self-assembled spheroidal grains densely embedded in a matrix, as seen in Fig. (1). This cut of a 3D microtomography image shows a sample with cylindrical shape of diameter about 7.4mm and height 2.6mm. It is discretized along $1500 \times 1500 \times 477$ greylevel points, or equivalently, voxels, with a resolution of 5.6μm per voxel. The large image size ensures both the representativness of the grains packing structure as well as good-enough resolution, as shown in a detail of the image in Fig. (2a). The average diameter of the grains in the propellant composite is known to be about 400 microns consistently with the microtomography in Fig. (1), where the high density of the tightly packed grains is conspicuous. Such microstructure is reminiscent of other man-made materials such as concrete or mortar [7] where self-assembled

gravels arrange in closely packed structures upon mixing for sufficiently long time. Intuitively, the high density somewhat constrains the number of possible configurations of the grains. The size of the typical length scale representative of the heterogeneous material is larger than the grains average diameter or of the same order depending in particular in the presence or absence of long-range correlations in the grains packing structure. The segmentation of the grains with respect to the matrix is required to answer such questions, and will be examined in more details in Sec. (IV). Furthermore, no macroscopic anisotropy is visible in the granular microstructure, i.e. although the grains shapes are anisotropic, no *privileged* direction appears. This point will likewise be investigated later when a segmented image is available.

As a pre-processing, a crop of size $926 \times 926 \times 463$ voxels is extracted from the middle of the cylinder in the original image, so as to remove the background entirely. The subsequent segmentation process described below is applied to this cropped image.

B. Image segmentation

Segmenting the image consists in first separating grains and matrix so as to obtain a binary representation of the composite at the level of the voxel. In this well contrasted image, this is straightforward by maximization of the interclass variance [24]. More precisely, the distribution of voxel intensities in the original image allows for an automatic thresholding as done in [7] in a similar context; the result is shown in Fig. 2b. The resulting segmentation might however not be sufficient for the purpose of this work, i.e. the computation of the local physical response of the material. The later possibly necessitates a description of the microstructure that is consitent with the connectivity of each grain, i.e. where grains are separated. In this respect, the information in the image itself is per se insufficient, as the gaps between neighboring grains are often smaller than the image resolution, leading to a more involved treatment. This second, possibly more accurate representation of the microstructure is derived from the original image by making each grain a connected component of the image, and separating them from their neighbours, as explained below.

C. Stochastic watersheds

So-called "stochastic watersheds" [1] are especially suited to the segmentation of granular microstructures of the type considered here, as they are aimed at unsupervised segmentation [23]. This consists in using a predefined number n of random markers to build a probability density function (PDF) of contours. In the case of granular materials, n is simply the number of grains contained in the image. In various applications, the latter has been automatically estimated. In [8], for instance, the covariance function together with the average radius of the grains and a Boolean model assumption [13] provides an estimate for n. The same method is used in the present work; it is emphasized that although the value of n is likely overestimated, as the grains do not interpenetrate, this does not affect the resulting segmentation. It should be noted that the original method introduced for computing the stochastic watershed is based on a large number of realizations of random markers to estimate a PDF of contours. The random markers are generated with a Poisson point process corresponding to a constant intensity. In the case of granular materials, a constant background marker, extracted by an automatic thresholding, is added to each set of random markers. The threshold is calculated via the maximization of the interclass variance [24].

Full segmentation is, accordingly, achieved in the following way. For each set of markers, a constrained watershed is computed. Then, the Parzen window is used to estimate the PDF of contours. From the PDF, it is possible to obtain the segmentation. The first approach used this PDF as a gradient

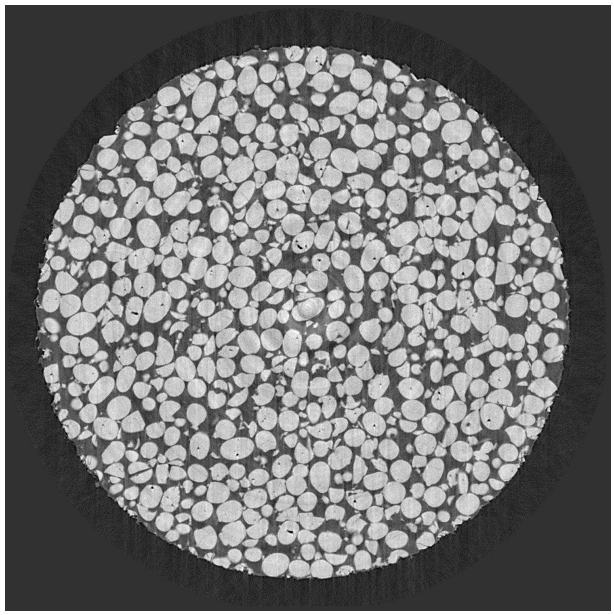
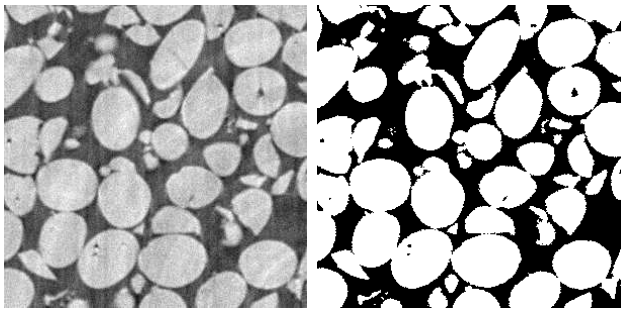


FIG. 1. 2D section of a 3D X-ray microtomography image of a sample of propellant butalite material .



(a) (b)

FIG. 2. Detail of a 2D section of a X-ray microtomography image of the granular material (a), and its corresponding segmentation by maximization of the interclass variance (b).

for a new watershed [1] whereas a more efficient method uses λ-flat zones to overcome the fact that the estimated PDF is not constant over each branch of contour [8]. Illustration of the PDF of contours is shown in Fig. (3a).



(a) (b) (c)

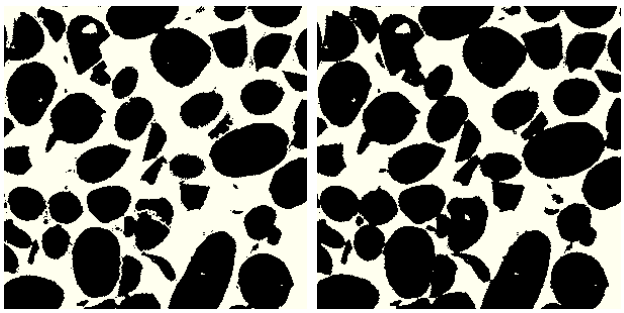
FIG. 3. Probability density function (PDF) of contours estimated with 50 realizations of a Poisson point process in 3D (a), computed with a graph-based approach (b) and graph-based stochastic watershed segmentation (c).

Although it provides good results, computing a large number of watersheds from simulations is a slow process, especially in 3D applications. A more efficient solution consists in using a graph-based approach [15, 27]. In the latter, the probability of boundaries is directly computed with a good approximation without resorting to realisations. More precisely, the method is as follow. A first watershed is computed from the local minima of the gradient, as is common in standard segmentation, but the latter is restricted to the complementary set of the background extracted by an automatic thresholding. For this purpose, the background is used as a marker. A very strong oversegmentation is obtained as a result of the presence of noise. From this watershed, an adjacency graph is built. Vertices of the graph are associated to each basin of the watershed, connecting edges between adjacent regions. A vertex is associated to the background too. Values are given to the vertices corresponding to the volumes of the regions. Each edge is labelled with the minimum of the gradient function on the boundary between the corresponding regions. From this valued graph, a minimum spanning tree is extracted [27]. Regions in the minimum spanning tree are afterward merged, starting with the edge of lowest value. After each merging, the probability p of the boundary between two regions V_1 and V_2 is estimated using [15]:

$$p = 1 - \left(1 - \frac{V_1}{V}\right)^n - \left(1 - \frac{V_2}{V}\right)^n + \left(1 - \frac{V_1 + V_2}{V}\right)^n, \tag{2.1}$$

i.e. it is set to the probability of obtaining at least one random marker in each of the two regions, knowing the volumes V_1 and V_2 of the two regions, the total volume V of the image and the number of markers n. It is seen from the equation above that the probability p increases with the volume of the grain. This may result in a bias towards largest grains if there exists a wide distribution of sizes in the image. After the merging of all the nodes in the original minimum spanning tree, the probability of all the edges of the tree is known. The result is projected from the tree on the graph and from the graph on the image. This approach provides uniform probability on each part of boundary between two regions, as illustrated on Fig. (3b). Therefore, a simple threshold can be used for the final segmentation as shown in Fig. (3c).

In the rest of this work, the resulting "Otsu" and "watershed" segmentations are respectively refered to as "connected" and "unconnected microstructures" (Fig. 4). In the former, the grains volume density is $f = 61.3\%$ on the sample, whereas in the latter $f = 53.7\%$.



(a) (b)

FIG. 4. Corresponding details of 2D sections of the "connected" (a) and "unconnected" (b) microstructures.

III. THERMAL AND ELASTIC CONSTITUTIVE LAWS

The thermal and linear elastic response of the propellant composite are investigated, under the classical assumption of quasi-static regime and small deformation:

$$q_i(\mathbf{x}) = -\lambda(\mathbf{x})\partial_i T(\mathbf{x}), \quad \partial_i q_i(\mathbf{x}) \equiv 0, \tag{3.1}$$

$$\sigma_{ij}(\mathbf{x}) = \mathbb{L}_{ij,kl}(\mathbf{x})\varepsilon_{kl}(\mathbf{x}), \quad \partial_i \sigma_{ij}(\mathbf{x}) \equiv 0, \tag{3.2}$$

$$\varepsilon_{ij}(\mathbf{x}) = \frac{\partial_i u_j(\mathbf{x}) + \partial_j u_i(\mathbf{x})}{2} \tag{3.3}$$

where $\mathbf{q}$ is the heat flux vector, T is the temperature, σ, ε and u are the stress and strain symmetric second-order tensors and the displacement vector, respectively. Furthermore, the local heat conductivity λ and elasticity tensor $\mathbb{L}$ are given by

$$\lambda(\mathbf{x}) = \begin{cases} 0.150 & (matrix) \\ 0.609 & (grains) \end{cases} \qquad \mathbb{L}_{ij,kl} = \mathbb{I}_{ij,kl} \times \begin{cases} 1 & (matrix) \\ 2 & (grains) \end{cases} \tag{3.4}$$

where $\mathbb{I}$ is the unity tensor associated to fourth-order tensors with major and minor symmetries. Values for the heat conductivity, expressed in J/(mKs), have been obtained experimentally, at a room temperature of 293K, whereas the elastic moduli are arbitrarily fixed. The unusual expression is equivalent to the arbitrary choice $2\mu = 3\kappa$ where μ and κ are the phases shear and bulk moduli. For both the elasticity and heat conductivity problems, the contrast of properties between grains and matrix is small, and of the same order. Accordingly, the elasticity problem acts as the mechanical counterpart of heat conductivity. It is emphasized that the two problems are uncoupled.

Periodic boundary conditions are considered to close the problems. For instance the heat flux and force acting along the faces between two unit cells $\mathbf{q}\cdot\mathbf{n}$ and $\sigma\cdot\mathbf{n}$, where $\mathbf{n}$ is the normal directed outwards, are anti-periodic. Equivalently, the segmented microstructure is used as the unit cell Ω of a periodic infinite medium over which a macroscopic field is applied. The microstructure along opposite faces of the unit cell obviously will not match, however the resulting border effects are known to be less than for classical static or kinematic boundary conditions [16]. Periodic boundary conditions include an average macroscopic field. Hereafter, a macroscopic temperature gradient $\Delta T^{(0)}$ is considered

$$\langle\partial_i T(\mathbf{x})\rangle = \Delta T^{(0)}\delta_{ij}, \quad j=1,2,3, \tag{3.5}$$

where δ_{ij} is the Kronecker symbol. Likewise hydrostatic or shear strain loadings are applied so that either

$$\langle\varepsilon_{ij}(\mathbf{x})\rangle = \varepsilon^{(0)}\delta_{ij}, \tag{3.6}$$

$$\langle\varepsilon_{ij}(\mathbf{x})\rangle = \varepsilon^{(0)}(\delta_{ik}\delta_{jl}+\delta_{il}\delta_{jk}), \tag{3.7}$$

$$\langle\varepsilon_{ij}(\mathbf{x})\rangle = \varepsilon^{(0)}(\delta_{ik}\delta_{jk}-\delta_{il}\delta_{jl}), \tag{3.8}$$

with $(k,l)=(1,2),(1,3),(2,3)$. In turn, the effective properties of the composite, with arbitrary anisotropy, are defined by :

$$\langle q_i(\mathbf{x})\rangle = -\lambda^{(0)}_{ij}\langle\partial_j T(\mathbf{x})\rangle, \quad \langle\sigma_{ij}(\mathbf{x})\rangle = \mathbb{L}^{(0)}_{ij,kl}\langle\varepsilon_{kl}(\mathbf{x})\rangle. \tag{3.9}$$

Full-fields solutions are readily computed using the Fast Fourier Transform method [22, 30], for both connected and unconnected composite structures. At low contrast of properties, convergence up to machine precision is achieved after a dozen of iterations.

IV. REPRESENTATIVE VOLUME ELEMENT AND EFFECTIVE PROPERTIES

The representative volume element (RVE) as well as the effective properties are investigated below for the connected microstructure. Results for the unconnected microstructures are very similar and are not repeated here. Regarding heat conductivity, the material is found to be macroscopically isotropic. FFT results for the apparent properties of the microstructure give :

$$\lambda^{(0)}_{11}=0.3888, \quad \lambda^{(0)}_{22}=0.3877, \quad \lambda^{(0)}_{33}=0.3864, \tag{4.1}$$

whereas $|\lambda^{(0)}_{ij}|<10^{-2}$ whenever $i\neq j$. Accordingly $\lambda^{(0)}_{ij}\approx\overline{\lambda}\delta_{ij}$ with $\overline{\lambda}\approx 0.387\pm 0.0015$. Hashin-Shtrikman's bounds indicate $0.368<\overline{\lambda}<0.415$ and the self-consistent scheme built on the Hashin-Shtrikman's variational formulation gives $\overline{\lambda}^{SC}\approx 0.4036$. The small difference $1-\overline{\lambda}^{SC}/\overline{\lambda}=0.04$ is an obvious consequence of the low contrast of properties, as the effective properties become microstructure independent in the limiting case of a infinitesimal contrast. One can notice that the effective conductivity is close to the lower Hashin-Shtrikman bound, as expected for granular media where the matrix percolates.

The integral range and representative volume element [16, 29] of the heat flux fields are readily determined from the numerical FFT solutions. When the overall volume Ω is subjected to a macroscopic temperature gradient, the variance of the heat flux field scales as:

$$D^2_{q_1}(V)\simeq\frac{D^2_{q_1}A_3}{|V|}, \tag{4.2}$$

where A_3 is the integral range and $D^2_{q_1}$ is the point variance of the field $q_1(\mathbf{x})$. In turn, the variance $D^2_{q_1}(\Omega)$ determines the absolute and relative precision on $\overline{\lambda}$. The scaling law for $D^2_{q_1}(V)$ is as predicted (Fig. 5). It is found that $A_3\approx 13^3$ voxels, $D^2_{q_1}\approx 0.23$ and that the relative error on $\overline{\lambda}$ is $\epsilon_{rela}=\delta\overline{\lambda}/\overline{\lambda}\approx 0.4\%$. The latter value is consistent with the variation observed on $\lambda^{(0)}_{11}$, $\lambda^{(0)}_{22}$ and $\lambda^{(0)}_{33}$. Similar conclusions are taken for the unconnected microstructure with effective conductivity of about $\overline{\lambda}^{u}\approx 0.3306\pm 0.002$. The effective properties are accordingly not sensitive to the connectivity properties of adjacent grains, the observed differences being almost exactly proportional to the volume fraction difference that results from the disconnection. This is due to the low contrast of conductivity between the grains and the matrix.

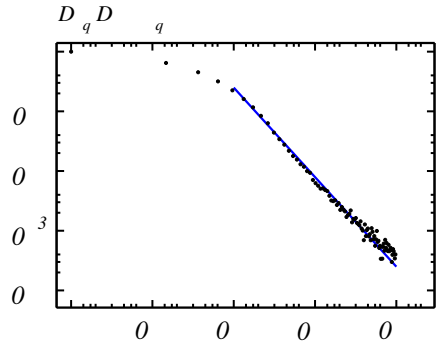


FIG. 5. Variance $D^2_{q_1}(V)$ of the heat flux field $q_1(\mathbf{x})$ over a subvolume V, as a function of the volume size $|V|$ in log-log scale (black points). The macroscopic gradient $\langle\partial_i T(\mathbf{x})\rangle=\Delta T^{(0)}\delta_{i1}$ is enforced over the whole volume Ω. The variance $D^2_{q_1}(V)$ is normalized by the point variance $D^2_{q_1}$; the ratio behaves as $\simeq A_3/|V|$ (blue curve) when $|V|$ is much larger than the integral range A_3.

Regarding linear elasticity, numerical computations are likewise consistent with a macroscopically isotropic material. FFT results indicate $\mu^{(0)}=0.6534$ and $\kappa^{(0)}=0.4455$ for the shear and bulk moduli, respectively, in good agreement with Hashin-Shtrikman's bounds. The latter read as $0.6457<\mu^{(0)}<0.6581$ and $0.4404<\kappa^{(0)}<0.4482$.

V. MAPS OF THE LOCAL THERMAL AND ELASTIC FIELDS

A. Thermal response

In this section, the local extrema of the heat and temperature fields are investigated using numerical full-fields computations on the whole sample. Although the effective properties of the composite are not sensitive to the microstructure in the present case, such may not be the case for the maximum value of the local fields. As shown in Fig. (6), the local heat flux exhibits hot spots located inbetween touching or almost touching grains. Such local maxima are also visible in the map of the temperature gradient (Fig. 7), albeit such local hot spots are restricted to the matrix phase. To investigate this property, 2D maps of the temperature gradient first component $\partial_1 T(\mathbf{x})$ are represented in Fig. (8). This component is parallel to the applied field, i.e. $\langle \partial_i T(\mathbf{x}) \rangle = \Delta T^{(0)} \delta_{i1}$. Hot spots zones where the $\partial_1 T$ field is a couple of times higher than $\lambda^{(m)} \Delta T^{(0)}$ are observed in the matrix, inbetween touching or almost touching inclusions, both for the connected (a) and unconnected microstructures (b). It is emphasized that such concentration zones are not the consequence of numerical artefacts due to the Fourier representation (i.e. Gibbs phenomenon). Indeed, as seen in Fig. (9), the hot spots locations are unaffected by lowering the resolution by a factor 2, where cubes of $2 \times 2 \times 2$ voxels are replaced by its top-left voxel.

As seen in Fig. 8, hot spot zones appear in the matrix along gaps located inbetween closely-packed grains with particular orientations. More precisely, the macroscopic applied field, oriented vertically in Fig. 8, is normal to the two grain boundaries delimiting hot spot zones. Furthermore, the hot spot intensity is smaller on the unconnected microstructure, suggesting it is highest when the distance between grains is minimal. To quantify such phenomenon, the hot spots of the $q_1(\mathbf{x})$ component are extracted by thresholding from the full-field map in Fig. (10). The threshold is readily determined using the variance of the field probability distribution $P_{\partial_1 T}(t)$ in the matrix (Fig. 11a). It is set to about $2\Delta T^{(0)}$, i.e. 2 times the field average in the whole volume. As seen in Fig. 11a, the pdf of the temperature gradient in the matrix shows a long tail for high values (up to seven times the average 1). The matrix is subsequently eroded by means of spheres of increasing diameter d. The ratio $V(d)/V(0)$ is used to compute the proportion of hot spots in volume in the eroded matrix compared to the initial volume of hot spots, or equivalently the proportion of points that belong to a hot spot at a distance larger than d of the matrix/grain boundary. It is shown in Fig. 12 for both the connected and unconnected microstructures. The sharp decrease shows that, accordingly to the maps, hot spots are located inbetween spheres that nearly touch grains. In this respect, a recent study [7] of the elastic response of a mortar with multiscale granulometry indicates that stress concentration zones are located preferentially inside cement, when gravels behave as quasi-rigid inclusions compared to cement.

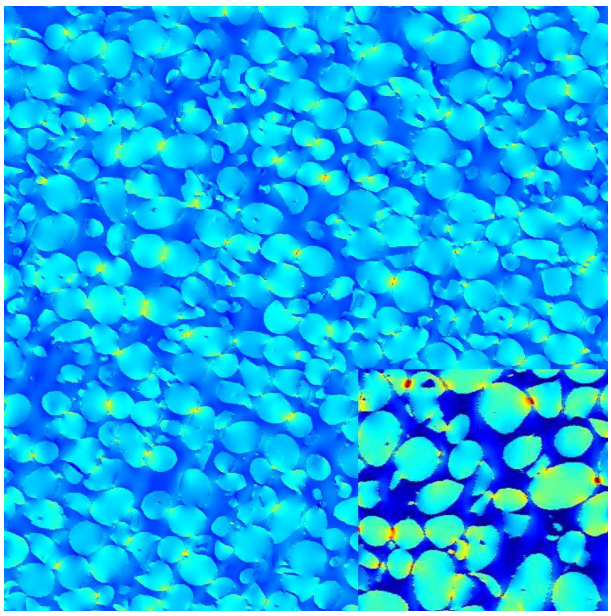


FIG. 6. 2D section of the heat flux component q_1+q_2 occurring in the granular microstructure with blue and red zones corresponding to the local minima and maxima, respectively (bottom right: enlarged detail). A macroscopic temperature gradient is applied along $(1,1,0)$, i.e. $\langle \partial_i T(\mathbf{x}) \rangle = \Delta T^{(0)}(\delta_{i1} + \delta_{i2})$. The minimum and maximum values are -2.1 and 7.4 respectively, when $\Delta T^{(0)} = 1$.

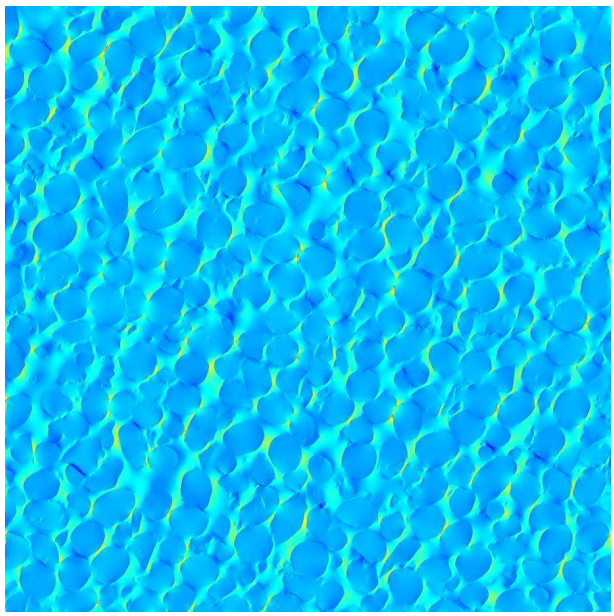
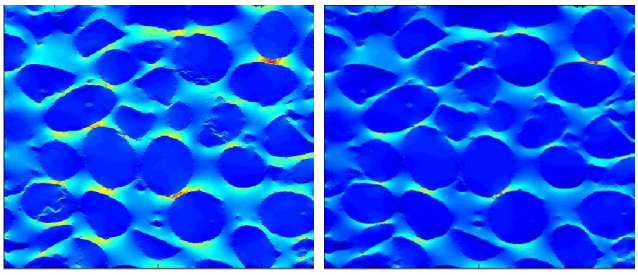


FIG. 7. 2D section of the temperature gradient component $(\partial_1 + \partial_2)T$ occurring in the granular microstructure with black and white zones corresponding to the local minima and maxima, respectively. A macroscopic temperature gradient is applied along $(1,1,0)$, i.e. $\langle \partial_i T(\mathbf{x}) \rangle = \Delta T^{(0)}(\delta_{i1} + \delta_{i2})$.



(a) (b)

FIG. 8. Maps of the temperature gradient component $\partial_1 T(\mathbf{x})$ along a 2D section $x_3 = cste$ with x_1 and x_2 directed downward and rightward, respectively, for the connected (a) and unconnected (b) microstructures. The component $\partial_1 T(\mathbf{x})$ is parallel to the applied field, i.e. $\langle \partial_i T(\mathbf{x}) \rangle = \Delta T^{(0)} \delta_{i1}$.

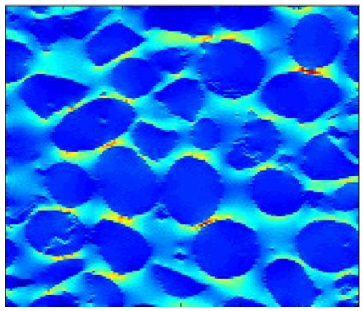


FIG. 9. Maps of the temperature gradient component $\partial_1 T(\mathbf{x})$ in the connected microstructure as in Fig. (8b) with resolution divided by 2. The component $\partial_1 T(\mathbf{x})$ is parallel to the applied field, i.e. $\langle \partial_i T(\mathbf{x}) \rangle = \Delta T^{(0)} \delta_{i1}$.

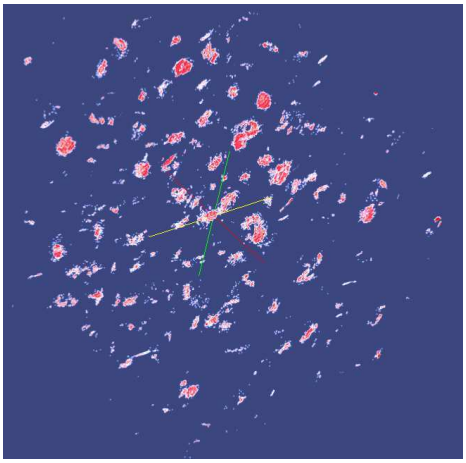


FIG. 10. 3D representation of hot spots found in the connected microstructure, obtained by thresholding.

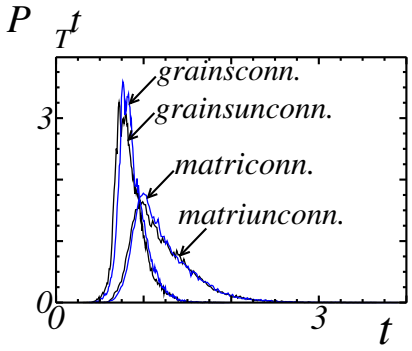


FIG. 11. Probability distribution $P_{\partial_1 T}(t)$ of the values of the temperature gradient component $\partial_1 T(\mathbf{x})$ in the grains and in the matrix (blue and black, respectively), for the connected and unconnected microstructures (labelled conn. and unconn., respectively). The component $\partial_1 T(\mathbf{x})$ is parallel to the applied field, i.e. $\langle \partial_i T(\mathbf{x}) \rangle = \Delta T^{(0)} \delta_{i1}$ with $\Delta T^{(0)} = 1$

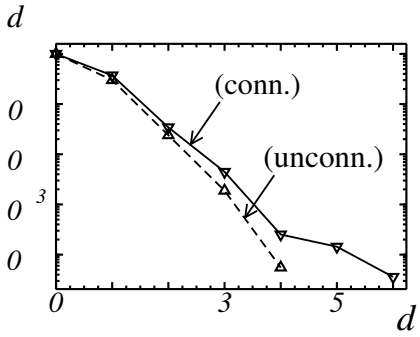
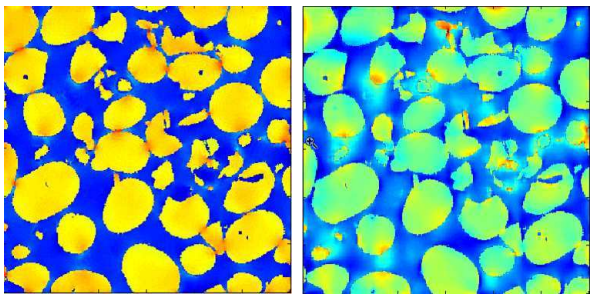


FIG. 12. Volume $W(d)$ of hot spots left in the matrix after an erosion of length d voxels, for the connected (conn.) and unconnected (unconn.) microstructures, as a function of d.

B. Elastic response

As per the linear elastic response, 2D sections of the local mean strain field $\varepsilon_m(\mathbf{x}) = (1/3)\varepsilon_{kk}(\mathbf{x})$ as well as of $\varepsilon_{12}(\mathbf{x})$ are represented in Fig. (13), with applied hydrostatic and shear strain loading. The two fields have non-zero average strain components. When hydrostatic strain loading is applied, local hot spots are likewise present inbetween touching or almost grains. However, contrary to the thermal case, the hot spots are not driven by any specific orientation and, accordingly, occur more frequently in the microstructure than for the temperature gradient. They also are much less pronounced than in thermal case. This is in agreement with results in [29, 30] where it was found that the typical sizes of the representative volume element is smaller in the mechanical problem than it is for conductivity, due to a lower variability of the fields in the elastic case. Finally, when shear loading is applied, as shown in Fig. (13b), the situation is much more involved. Although, the strain field is maximum along matrix/grain boundaries, the

location of the extrema depends on both the local orientation and shape of the inclusions.



(a) (b)

FIG. 13. Maps of the mean and shear strain components ε_m (a) and ε_{12} (b), with applied hydrostatic strain loading $\varepsilon_{ij}(\mathbf{x})\rangle = \varepsilon^{(0)}\delta_{ij}$ and shear along $1,2$, $\varepsilon_{ij}(\mathbf{x})\rangle = \varepsilon^{(0)}(\delta_{i1}\delta_{j2}+\delta_{i2}\delta_{j1})$, respectively. The local fields maxima are shown in red, whereas smallest values are in blue.

VI. SMALL CONTRAST OF PROPERTIES

A. Local extrema

The limiting case of an infinitesimaly small contrast of properties is investigated in order to assess the observed properties of the thermal fields extrema. Consider a microstructure made of two phases of heat conductivity $\lambda(\mathbf{x}) = \lambda^{(m)}$ in a "matrix" and $\lambda(\mathbf{x}) = (1+h)\lambda^{(m)}$ in "inclusions", with $h \ll 1$. A macroscopic temperature gradient $\Delta T^{(0)}\delta_{i1}$ is applied along axis 1. The local temperature gradient and heat flux fields are expanded with respect to h, when $h \ll 1$, as

$$\partial_i T(\mathbf{x}) = A_i^{(0)}(\mathbf{x}) + hA^{(1)}(\mathbf{x}) + O(h^2), \tag{6.1}$$

$$q_i(\mathbf{x}) = B_i^{(0)}(\mathbf{x}) + hB_i^{(1)}(\mathbf{x}) + O(h^2). \tag{6.2}$$

Expanding $\lambda(\mathbf{x})\partial_i T(\mathbf{x})$ in terms of h, it is found that, assuming sufficient conditions of regularity for the terms in $O(h^2)$

$$A_i^{(0)}(\mathbf{x}) = B_i^{(0)}(\mathbf{x})/\lambda^{(m)} \equiv \Delta T^{(0)}\delta_{i1}, \tag{6.3}$$

$$B_i^{(1)}(\mathbf{x}) = \lambda^{(m)}\chi(\mathbf{x})\Delta T^{(0)}\delta_{i1} + \lambda^{(m)}A_i^{(1)}(\mathbf{x}) \tag{6.4}$$

where $\chi(\mathbf{x})$ is the characteristic function of the inclusions. Furthermore, under conditions of regularity for the terms in $O(h^2)$ in Eq. (6.2), the fields $\mathbf{A}^{(1)}$ and $\mathbf{B}^{(1)}$ satisfy the admissibility and equilibrium conditions, i.e. we have $curl A^{(1)} = 0$ and $div B^{(1)} = 0$. The fields $\mathbf{A}^{(1)}$ and $\mathbf{B}^{(1)}$ also satisfy periodic boundary conditions, together with the macroscopic condition $\langle A_i^{(1)}\rangle = 0$. Hence, their solutions are given by the Lippmann-Schwinger's equations

$$A_i^{(1)}(\mathbf{x}) = -\lambda^{(m)}\Delta T^{(0)}\int \mathrm{d}^d\mathbf{x}'^{(m)} G_{i1}^{(0)}(\mathbf{x}'-\mathbf{x})\chi(\mathbf{x}'), \tag{6.5}$$

where $\mathbf{G}^{(0)}$ is the second-order Green operator associated to $\lambda^{(m)}$. Not surprisingly, the above equation is "linear" in terms of the microstructure, i.e. it is linear in $\chi(\mathbf{x})$. Accordingly, the local temperature gradient field is, at first order in h, the sum of the applied macroscopic field $\Delta T^{(0)}\delta_{i1}$ and of the perturbations induced by all inclusions separately, neglecting pairs and other higher-order interactions. It is noted that, for a single sphere of radius 1 and center at coordinates 0 in an infinite medium, the heat flux outside the inclusion reads:

$$q_i^{(sphere)}(\mathbf{x}) = \lambda^{(m)}\Delta T^{(0)}\left[\delta_{i1} - \frac{h}{3+h}\frac{1}{r^3}\left(\delta_{i1}-3n_1n_i\right)\right], \tag{6.6}$$

where $r = |x| = \sqrt{x_1^2+x_2^2+x_3^2}$ and $n_i = x_i/r$. Inside the inclusion ($r \leq 1$) the heat flux is constant with $q_i^{(sphere)}(\mathbf{x}) = 3(1+h)/(3+h)\lambda^{(m)}\Delta T^{(0)}$. Accordingly, the perturbating heat flux component q_1 generated by two closely packed inclusions add up when their centers are oriented in the direction of the applied field (see Fig. 14), whereas they cancel if they are oriented in a direction normal to it. In the two spheres model, the maximum of the heat flux is located along the matrix/inclusion boundary. In the limiting case of touching spheres, the field becomes in the gap between the two inclusions, with heat flux value $q_1^{(max)} = \lambda^{(m)}\Delta T^{(0)}(1+4h/3)$ at first order in h. Additionally, in the two-spheres solution at low contrast, the minimum of the heat field component q_1 occurs in the gap inbetween the two spheres when the applied macroscopic field is normal to the line joining the sphere centers. For such configuration, the minimum heat field is $q_1^{(min)} = \lambda^{(m)}\Delta T^{(0)}(1-2h/3)$ at first order in h. This is indeed seen in the map of Fig. (6), although such "cold spots" are, accordingly to the anlytical formula, less visible than hot spots.

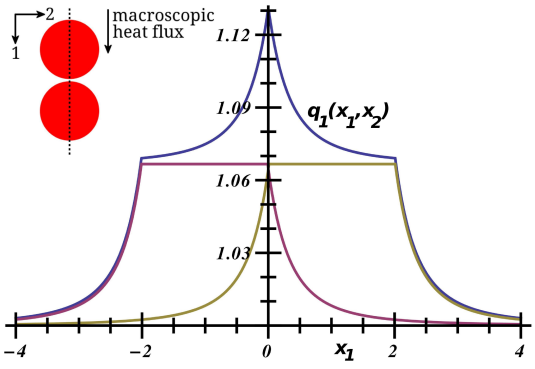


FIG. 14. Heat flux component $q_1(x_1,x_2)$ (blue curve) along the line $x_2 = cst$ passing through the centers of two closely-packed spheres (dotted line, top-right) as a function of the coordinate x_1, in the case of a smal contrast between the spheres and the matrix conductivity set to $\lambda^{inc}/\lambda^{(m)} = 1.1$. Shown in red and brown are the contributions of each sphere, equal to the heat flux component q_1 if the sphere was alone in the matrix. The sphere diameter is equal to 1 and the distance between the two spheres is set to 0.01. A macroscopic heat flux is applied far from the spheres so that $\langle q_i(x_1,x_2)\rangle = \delta_{i1}$.

B. Trial field

To investigate the range of validity, in terms of the contrast h, of the above results, a trial field is used to compute an estimate of the maximum of the heat flux field in the matrix. The first-order correction field $\mathbf{A}^{(1)}(\mathbf{x})$ computed above is used to introduce the trial temperature gradient field:

$$\mathbf{E}^*(\mathbf{x};t) = \Delta T^{(0)}\delta_{i1} + t\mathbf{A}^{(1)}(\mathbf{x}), \tag{6.7}$$

where t is optimised to minimize the energy density $W(t) = \frac{1}{2}\langle\lambda(\mathbf{x})\,[E_i^*(\mathbf{x})]^2\rangle$. It is found that

$$t = -\Delta T^{(0)}\frac{\langle\lambda(\mathbf{x})A_1^{(1)}(\mathbf{x})\rangle}{\langle\lambda(\mathbf{x})A_i^{(1)}(\mathbf{x})A_i^{(1)}(\mathbf{x})\rangle}. \tag{6.8}$$

Formula (6.7) and (6.8) are applied to a simple 2D Boolean model of cylinders, to compute an estimate of the maximum of the heat flux field $q_1(\mathbf{x})$ at increasing contrasts h, and compared with FFT results. At low contrast $h \ll 1$, Eq. (6.8) reduces to $t \approx h$; at moderate contrasts however the choice of Eq. (6.8) for t somewhat improves the range of validity of the trial field for computing the maximum local heat flux up to $h \approx 10$ (where the error is less than 4%, see Fig. 15). At infinite contrasts, the scalar t tends to a finite value resulting in a finite limit for the maximum of the temperature gradient $\mathbf{E}^*(\mathbf{x};t)$ (not shown), but to an infinite value for the maximum of the heat flux, contrary to FFT results.

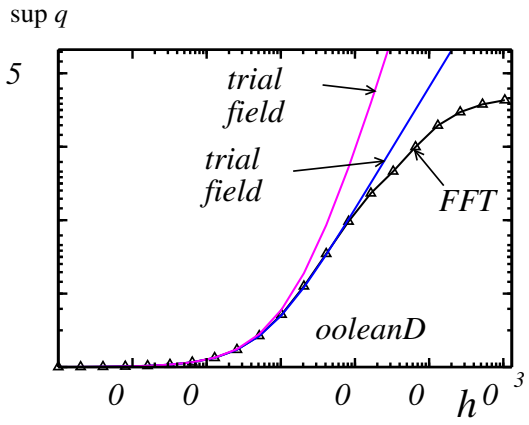


FIG. 15. Maximum of component 1 of the heat flux $q_1(\mathbf{x})$ in the matrix and inclusions as a function of the contrast h in log-log scale, for a Boolean set of cylinders of concentration 30%: comparison between FFT results and estimate given by the trial fields $\mathbf{E}^*$ from Eq. (6.7) with the choice $t = h$ (trial field 1, magenta) or t as in Eq. (6.8) (triald field 2, blue). A macroscopic temperature gradient is applied in direction 1 so that $\langle\partial_i T(\mathbf{x})\rangle = \partial_{i1}\Delta T^{(0)}$ with $\Delta T^{(0)} = 1$. When h is small, the maximum of the heat flux $q_1(\mathbf{x})$ behaves as $\approx 1 + 1.4h$, close to the trial fields prediction, and tends to the finite value ~ 181 when $h = +\infty$, whereas the trial field estimates predict an infinite value.

VII. HARD-CORE MODEL OF CYLINDERS

In the following section, a hard-core model of cylinders (Fig. 16) is considered. The choice of a $2D$ model is necessary to get accurate FFT results on large image size and high resolution of gaps inbetween closely packed grains. For the purpose of this study, the distribution of distances between neighboring inclusions in the hard-core model should not be concentrated around a few values but, ideally, close to a uniform distribution between 0 and a maximum. To achieve this, the procedure for adding cylinders is as follows. The first cylinders are placed randomly as long as no interpenetration occurs, this process being repeated until 15 of them have been included in the image. Subsequent cylinder are added in the following way. Additional cylinders are initially placed randomly. If no interpenetration occurs with the other cylinders, the cylinder is moved in a random direction until it touches a cylinder, and, finally, moved back in the opposite direction by a random length taken uniformly between 0 and a maximum value. If on the contrary interpenetration occurs with the other cylinders, the cylinder is moved in a random direction until it is completely included in the matrix, then moved again in the same direction by a random length taken uniformly between 0 and a maximum value. At the end of this process, it is checked if the cylinder intersects an already placed cylinder in its final position. The cylinder is finally kept if no interpenetration occurs. It is noted that the resulting distribution of gaps is not uniform, as the procedure does not take into account situations where the cylinder is close to several other cylinders in different directions. Although such situations become frequent when the cylinder density is high, the procedure nevertheless results in a distribution of gaps where all distance values are represented.

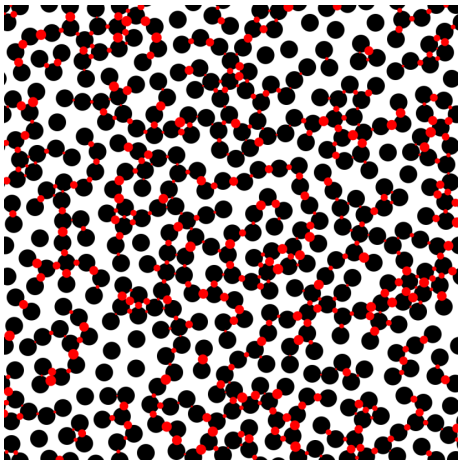


FIG. 16. Hard-core model of cylinders with gaps between neighboring inclusions shown in red.

VIII. NETWORK APPROXIMATION AT INFINITE CONTRAST

Although several analytical methods have been proposed to compute the full-field thermal response of a pair of interacting spheres [12, 21], such solutions are generally expressed in terms of infinite series. However, as the contrast of properties increase and the distance betwen inclusions tends to 0, the number of terms in the series that are necessary to compute the local fields tends to infinity. In the limiting case of touching inclusions, the boundaries of the two cylinders delimiting the gap are quasi parallel planes. Accordingly, the heat flux is tantamount to that found in a laminate material and the heat flux field is directed along the normal of the boundaries. Furthermore, it does not depend on the coordinate along the normal of the boundary, but only to the transverse coordinate. Thus, the local heat flux may be written as $q_i(\mathbf{x}) = [q_j(\mathbf{x}-\mathbf{x}\cdot\mathbf{n})n_j(\mathbf{x})]n_i(\mathbf{x})$ with $q_j(\mathbf{x})n_j(\mathbf{x}) = q_n(x_t)$ where q_n is the component of the heat flux in the direction normal to the boundary, directed from inclusion 1 to 2, and x_t is the coordinate along the direction parallel to the boundary. Minimizing the energy density $(1/2)\int q_i\partial_i T$ results in the following form

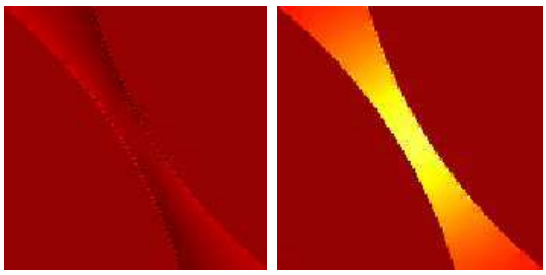
$$q_n(\mathbf{x}) = \frac{\lambda^{(m)}\left[T^{(1)} - T^{(2)}\right]}{\delta + 2\left(a - \sqrt{a^2 - x_t^2}\right)}, \tag{8.1}$$

if $T^{(1)}$ and $T^{(2)}$ are the temperatures of the inclusions, δ and a are the distance between inclusions and radius disks, respectively. Very good match (up to the discretisation employed for the disks boundary) is found with numerical FFT computations (see Fig. 17 and 18). Integrating the heat flux along the gap results in the following form:

$$q^{(1,2)} = \Lambda^{(1,2)}(T^{(1)} - T^{(2)}), \tag{8.2}$$

$$\Lambda^{(1,2)} = \frac{\lambda^{(m)}}{2}\int_{x_t}\frac{\mathrm{d}\,x_t}{\delta/2 + a - \sqrt{a^2 - x^2}}, \tag{8.3}$$

where $q^{(1,2)}$ is the total heat flux going from inclusion 1 to 2 and $\Lambda^{(1,2)}$ is an equivalent gap conductivity. When $\delta \to 0$ the formula $\Lambda^{(1,2)} = \pi/\sqrt{\delta/a}$ is recovered. Accordingly, the set of closely packed disks may be replaced by an equivalent network where vertices are gaps between inclusions, and inclusions are nodes. The vertices conductivity is given by Eq. (8.3) and the equilibrium condition at each node is used to compute the temperature in each inclusion. Equivalent network mappings have been considered for similar microstructure models and extensively studied [2, 9, 18], however the validity of such models has been recently questioned by [5]. It should be noted that the derivation of the local fields in the gap undertaken here gives information as to the local extrema inside the gaps occurring at $x_t = 0$, where indeed, $q_n(\mathbf{x}) = q_n^{(max)} = \lambda^{(m)}(T^{(1)} - T^{(2)})/\delta$. In Fig. (19) the periodic part of the temperature field, where variations are most noticeable are shown. Comparisons are made between the fields predicted by the network mapping and full-fields FFT computations. The local extrema of the field computed by means of FFT requires very high resolution and stabilizes only for microstructures of sizes larger than $10,000^2$ voxels (the heat field maxima is 29.5 and 30.2 for resolution $10,000^2$ and $50,000^2$). Although the two field maps in Fig. (19) are similar, small differences occur at certain places, which are, in turn, responsible for high differences between the maximum value of the heat field as predicted by the network mapping and full-field FFT computations. More precisely, the maximum value is overestimated by a factor 4 with the network mapping. Accordingly, even though the temperature field is well predicted by the network mapping, on average, no such conclusion is drawn for the heat field extreme values. The hypothesis of infinitesimal gaps in the network mapping may be insufficient when handling a dispersion of the gap widths, although additional studies are needed to investigate the model.



(a) (b)

FIG. 17. Transverse (a) and normal (b) components of the heat flux vector occurring in a gap located inbetween two randomly oriented, closely-packed infinitely-conducting inclusions. The transverse component in (a), orthogonal to the inclusion frontiers in the gap, is close to 0 (brown) whereas the normal component in (b), parallel to the inclusion frontiers, is close to a field that, in the matrix, depends solely on the transverse coordinate (in yellow-red colors).

IX. CONCLUSIONS

In this work, thresholding by means of the Otsu and stochastic watershed method were used to succesfully segment and separate the grains in a large, 3D microtomography image of a granular microstructure. At low contrast of properties, the effective thermal and elastic properties of the composite have been readily computed by means of FFT computations, with a high precision of less than 0.4%. Accordingly, the image is very acceptable representative volume element. The local heat field computed numerically includes hot spots (as well as cold spots) where the heat flux attains a local extremum (respectively a minimum). Along these hot spots, the field local fluctuations are much larger than that of the mean field fluctuations, and proportional to the contrast of properties between the grains and the matrix. These hot spots, present even for a low contrast of properties between the grains and the matrix, are induced by the microstructure; more precisely, they occure in gaps located inbetween closely packed spheroidal inclusions. The latter are a local phenomenon, in the sense that they are driven by the two

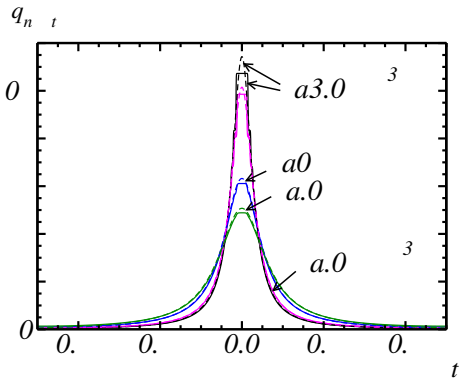


FIG. 18. Behavior of the heat flux component q_n normal to the boundaries of two closely-packed perfectly-conducting discs of radius a, as a function of the coordinate x_t parallel to the boundaries, as observed in Fig. (17b): comparison between analytical results in Eq. (8.1) (dotted lines) and FFT computations (solid lines), for varying normalized distances $\delta/a = 3\,10^{-3}$, $4\,10^{-3}$, 10^{-2} and $2\,10^{-2}$. The "stair-shaped" solid curves are an effect of the disc discretization when δ/a is small and x_t is close to 0.

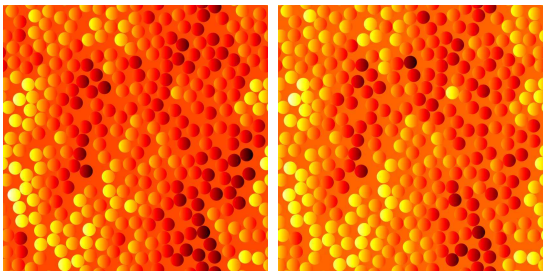


FIG. 19. Periodic part of the temperature field $T(\mathbf{x}) - \Delta T_i^{(0)} x_i$ in the hard-core Boolean model with infinitely-conducting cylinders. Comparison between FFT exact results and the "network model", with highest and lowest values shown in white and red, respectively.

nearby inclusions and not by the packing structure at larger length scales. In the thermal problem, hot spots appear along boundaries where the macroscopic applied field is normal to the boundaries. Additionally, the maximum value of the heat field in the hot spot increases when the distance between inclusion decreases (see e.g. [11] for a similar study in the context of electrostatic and a periodic structure). Such results are generalized in the case of linear elasticity with hydrostatic strain loading, but not when shear loading is applied. In the former, however, the stress maximum value are located in-between closely packed grains, irrespective of their orientations, and the hot spots are comparatively softened. Analytical derivations and network based mappings tend to precise the behavior of the local field extrema for varying contrasts of properties. In the infinitely contrasted media, the situation is much more sensitive to the microstructure and no analytical or semi-analytical method proved to give good estimates. In the presence of friction, hot spots such as the ones described in this study could initiate uncontrolled explosion in propergol materials from local ignition [4, 6, 10, 28]. These hot spots are prone to appear in a thermal gradient, even in the absence of shock [3].

Acknowledgments: This work was supported by a grant fom DGA (contract 2009 34 0006). The authors are grateful to Alain Fanget (CEA Gramat) for his advice during this study.

[1] Angulo, J., Jeulin, D., 2007. Stochastic watershed segmentation. Proc. of ISMM'2007, 8^{th} International Symposium on Mathematical Morphology, Rio de Janeiro, Brazil, 265-276.

[2] Berlyand, L., Kolpakov, A., 2001. Network approximation in the limit of small interpartcile distance of the effective properties of a high-contrast random dispersed composite. Arch. Rational Mech. Anal. 159, 179–227.

[3] Bennett, J. G., Haberman, K. S., Johnson, J. N., Asay, B. W., 1998. A constitutive model for the non-shock ignition and mechanical response of high explosives. J. of the Mech. and Phys. of Sol. 46, 12, 2303-2322.

[4] Bonnett, D. L., Butler, P. B., 1996. Hot-spot ignition of condensed phase energetic materials. J. of Propulsion and Power. 12, 4, 680-690.

[5] Chen, Y., Schuh, C. A., 2009. Effective transport properties of random composites: continuum calculations versus mapping to a network. Phys. Rev. E 80, 0401103.

[6] Elban, W. L., Hoffsommer J. C., Coffey, C. S., Yoo, K. C., Rosemeier, R. G., 1984. Microstructural origins of hot spots in RDX explosives and a reference inert material. NSWC (Naval Weapons Surface Center) 84-200.

[7] Escoda, J., Willot, F., Jeulin, D., Sanahuja J., Toulemonde, C., 2011. Estimation of local stresses and elastic properties of a mortar sample by FFT computation of fields on a 3D image. Cement and Concrete Research 41, 5, 542-556.

[8] Faessel, M., Jeulin, D., 2010. Segmentation of 3D microtomographic images of granular materials with the stochastic watershed. J. of Microscopy 239, 1, 17-31.

[9] Feng, S., Halperin, B. I., Sen, P. N., 1987. Transport properties of continuum systems near the percolation threshold. Phys. Rev. B. 35, 197-214.

[10] Field, J. E., Bourne, N. K., Palmer, S. J. P., Walley, S. M., Sharma, J., Beard, B. C., 1992. Hot-Spot Ignition Mechanisms for Explosives and Propellants [and Discussion]. Phil. Trans. R.

Soc. Lond. A 339, 1654, 269-283.

[11] Fleger, Y., Rosenbluh, M., Strelniker, Y. M., Bergman D. J., Lagarkov A. N., 2011. Controlling the optical spectra of gold nano-islands by changing the aspect ratio and the inter-island distance: theory and experiment. Eur. Phys. J. B 81, 1, 85-93.

[12] Jeffrey, D. J., 1978. The temperature field or electric potential around two almost touching spheres. J. Inst. Maths Applics 22, 337-351.

[13] Jeulin, D., 1991. Modèles morphologiques de structures aléatoires et de changement d'échelle. Thèse de Doctorat d'État, University of Caen, France.

[14] Jeulin, D., Li, W., Ostoja-Starzewski, M., 2008. On the geodesic property of strain field patterns in elastoplastic composites. Proc. of the R. Soc. A 464, 2093, 1217-1227.

[15] Jeulin D., 2008. Remarques sur la segmentation probabiliste. N-10/08/MM, Internal Report, Mines ParisTech.

[16] Kanit, T., Forest, S., Galliet, I., Mounoury, V., Jeulin, D., 2003. Determination of the size of the representative volume element for random composites: statistical and numerical approach. Int. J. of Sol. and Struct. 40, 13.

[17] Keller, J. B., 1963. Conductivity of a medium containing a dense array of perfectly conducting spheres or cylinders or non-conducting cylinders. J. of Appl. Phys. 34, 991.

[18] Kerstein, A. R., 1983. Equivalence of the void percolation problem for overlapping spheres and a network problem. J. Phys. A: Math. Gen. 16, 3071-3075.

[19] McPhedran, R. C., 1986. Transport properties of cylinder pairs and of the square array of cylinders. Proc. R. Soc. Lond. A 408, 31-43.

[20] McPhedran, R. C., Milton, G. W., 1987. Transport properties of touching cylinder pairs and of the square array of touching cylinders. Proc. R. Soc. Lond. A 411, 313-326.

[21] Poladian, L., McPhedran, R. C., Milton, G. W., 1988. Asymptotic studies of closely spaced, highly conducting cylinders. Proc. R. Soc. Lond. A 415, 185-196.

[22] Moulinec, H., Suquet, P., 1994. A fast numerical method for computing the linear and nonlinear mechanical properties of composites. C. R. Acad. Sc. 318, 1417.

[23] Noyel, G., Angulo, J., Jeulin, D., 2010. Regionalized Random Germs by a Classification for Probabilistic Watershed Application: Angiogenesis Imaging Segmentation. Progress in Industrial Mathematics at ECMI 2008, Mathematics in Industry 15, 2, 211-216, 2010.

[24] Otsu, N., 1979. A threshold selection method from gray-level histograms. IEEE Trans. Sys. Man. Cyber. 9, 62-66.

[25] Prakash, A., Lebensohn, R. A., 2009. Simulation of micromechanical behavior of polycristals: finite element versus fast Fourier transforms. Model. and Simulation in Materials Sc. and Eng. 18, 064010.

[26] Rolett, A. D., Lebensohn, R. A., Groeber, M., Choi, Y., Li, J., Rohrer, G. S., 2010. Stress hot spots in viscoplastic deformation of polycristals. Model. and Simulation in Materials Sc. and Eng. 18, 074005.

[27] Stawiaski, J., Meyer, F., 2010. Stochastic watershed on graphs and Hierarchical Segmentation. Proc. of the European Conference on Mathematics for Industry (ECMI), Wuppertal, Germany.

[28] Tarver, C. M., Chidester, S. K., Nichols A. L., 1996. Critical Conditions for Impact- and Shock-Induced Hot Spots in Solid Explosives. J. Phys. Chem. 100, 14, 5794–5799.

[29] Willot, F., Jeulin D., 2009. Elastic behavior of composites containing Boolean random sets of inhomogeneities. Int. J. of Eng. Sc. 4, 2.

[30] Willot, F., Jeulin, D., 2011. Elastic and electrical behavior of some random multiscale highly-contrasted composites. Int. J. of Multiscale Comp. Eng. 3, 305-326.